Adaptive Mesh Optimization for Simulation of Immiscible Viscous Fingering

Peyman Mostaghimi[1], SPE, Fatemeh Kamali[1], SPE, Matthew D. Jackson[2], SPE, Ann H. Muggeridge[2], SPE, Christopher C. Pain[2]
[1]School of Petroleum Engineering, The University of New South Wales, Australia
[2]Department of Earth Science and Engineering, Imperial College London, United Kingdom

Abstract

Viscous fingering can be a major concern when waterflooding heavy oil reservoirs. Most commercial reservoir simulators employ low-order finite volume/difference methods on structured grids to resolve this phenomenon. However, this approach suffers from a significant numerical dispersion error due to insufficient mesh resolution which smears out some important features of the flow. We simulate immiscible incompressible two-phase displacements and propose the use of unstructured control volume finite element (CVFE) methods for capturing viscous fingering in porous media. Our approach uses anisotropic mesh adaptation where the mesh resolution is optimized based on the evolving features of flow. The adaptive algorithm uses a metric tensor field based on solution interpolation error estimates to locally control the size and shape of elements in the metric. The mesh optimization generates an unstructured finer mesh in areas of the domain where flow properties change more quickly and a coarser mesh in other regions where properties do not vary so rapidly. We analyze the computational cost of mesh adaptivity on unstructured mesh and compare its results with those obtained by a commercial reservoir simulator based on the finite volume methods.
Key words: Viscous fingering, Mesh adaptivity, Porous media, Immiscible flow, Numerical simulation

Introduction

Viscous fingering, also known as Saffman-Taylor instability, is an instability that occurs during unfavorable, mobility ratio displacements, when a more viscous fluid is displaced by another fluid that is less viscous (Saffman and Taylor,1958). It can be of major concern in several oil recovery processes including waterflooding of heavy oil reservoirs and miscible and immiscible gas injection as it results in reduction in the sweep efficiency and an early breakthrough of the displacing fluid (Lake, 1989). It is therefore important to be able to predict when viscous fingering occurs and how it develops. The criteria for instability in immiscible displacements is much stronger as in these cases it is necessary for the shock front mobility ratio to be greater than 1 (Chuoke, 1959).

The number and growth rate of the fingers are controlled by the level of physical diffusion (capillary pressure in immiscible displacements) between the injected and displaced fluid (e.g. Chikhliwala et al., 1988; Christie, 1989; Riaz and Tchelepi, 2006). Fingering will only occur is miscible displacements when the viscosity ratio is greater than 1. It is therefore important to ensure that the physical diffusion in a simulation is greater than the numerical diffusion. For most field-scale displacements this requires a prohibitively large number of cells, especially if using a conventional, first order, finite volume approach. A further problem is that significant grid orientation error can occur when using such approaches (e.g. Djjabarov et al., 2016).

A range of numerical approaches have been applied to this problem with the aim of minimizing numerical diffusion and grid orientation error. There is a significant literature on the numerical modeling of first contact miscible viscous fingering, most showing that conventional finite volume approaches are very successful for linear displacements. Tan and Homsy (1988) developed a spectral method to study the dynamics of viscous fingering however they found the method resulted in numerical instabilities at high Peclet and Reynolds numbers. Christie and Bond (1987) developed a more conventional, higher order, finite difference method for capturing miscible viscous fingering. The method was validated by comparing predictions against the experimental data of Blackwell et al. (1959). Subsequent works (Christie and Jones, 1987; Christie et al. 1989; Davies et al. 1991; Muggeridge et al., 2002) have shown this approach can successfully predict first contact miscible fingering patterns, solvent production and oil recovery obtained from physical experiments performed under a range of conditions, with and without gravity, and including well-characterized heterogeneities. Araktingi and Orr (1990) developed a particle-tracking simulator to study the combined effects of permeability heterogeneity, flow rate and mobility ratio on miscible viscous fingering. They obtained a good agreement when they compared their numerical results with experimental results from the literature. Tchelepi and Orr (1994) developed this particle-tracking approach into a hybrid finite difference and particle tracking technique. They used this approach to compare results obtained from two- and three-dimensional simulations of viscous fingering with the specific objective of investigating the impact of gravity on finger growth. A finite element model was developed by Kelkar and Gupta (1991) with the aim of reducing both numerical diffusion and grid orientation error. De Wit and Homsy (1997) performed numerical simulations based on Fourier spectral method (Tan and Homsy, 1988) to study viscous fingering in periodically heterogeneous porous media. They compared and contrasted the

dynamics of fingers with those occurring in homogeneous medium and showed qualitative agreement with experimental visualizations. More recently, Ruith and Meiburg (2000) developed a vorticity-stream function formulation to investigate the influence of the Peclet number, viscosity and density contrast, and the aspect ratio on the dynamic evolution of displacement in porous media.

The literature investigating methods for the numerical simulation of immiscible viscous fingering is much more limited and suggests that it is much harder to model the dynamics of immiscible viscous fingering using conventional finite volume approaches. Riaz and Tchelepi (2006) applied the vorticity-stream function formulation to solve for velocity using Fourier-Galerkin spectral method and investigated the effect of the relative permeability functions on viscous fingering. Riaz et al. (2007) extended these studies to compare the method to laboratory experiments investigating viscous fingering in a sandstone core but were not able to obtain good agreement with the experiments. Daripa and Pasa (2008) studied instability of immiscible displacement in the presence of capillary pressure and showed that the slowdown of instability by capillarity is commonly very rapid. Berg and Ott (2012) studied the stabilizing influence of capillary pressure using a finite volume method and triggered fingers by superimposing a permeability variation on the domain. Jauré et al. (2014) have developed a higher order simulator based on the multipoint flux approximation that is readily parallelizable and applied this to the modeling of the experiments described by Riaz et al. (2007).

All of the above approaches used static meshes meaning that a fine resolution was required throughout the domain to capture the development of the fingers accurately. Such fine meshes mean that the simulations are both CPU and memory intensive. This is wasteful of computing resources as the fine resolution is only needed in the vicinity of the viscous fingers. Properties such as saturation or concentration only change slowly, if at all, ahead of and behind the fingers. Although some existing commercial reservoir simulation software provides the facility to automatically develop non-uniform static meshes, they are not able to dynamically adapt the mesh during the simulation. Implementing dynamic adaptive meshing would enable computational effort to be focused where it is most needed, minimizing CPU time whilst also minimizing numerical diffusion. Edwards and Christie (1993) and Mulder and Gmeling Meyling (1993) both proposed using dynamic and adaptive meshes for the modeling of first contact miscible viscous fingering but only in a finite volume model. These models were able to reduce numerical diffusion but the models were still prone to grid orientation error.

We propose using dynamic mesh adaptivity and control volume finite element (CVFE) methods to resolve viscous fingering in reservoir flows. The CVFE approach means that the simulations will be less subject to grid orientation error whilst the dynamic mesh adaptivity means that a high resolution mesh can be used to resolve the fingers whilst coarsening the mesh in other regions. The method is used to simulate immiscible incompressible two phase displacements in two dimensional porous media and the results are compared with those obtained using fixed mesh in a commercial reservoir simulator based on the finite volume method. Capillary pressure is neglected in all these simulations in order to focus on the comparison of the differences in numerical diffusion and grid orientation error seen in the different modeling approaches. The remainder of this paper is organized as follows. The next section reviews the governing equations of immiscible and incompressible flow in porous media. Then, we describe the applied adaptive mesh CVFE numerical techniques used to simulate viscous fingering in this study. Finally, we present several numerical models and demonstrate the capabilities of mesh adaptivity for simulation of viscous fingering.

Mathematical Formulation

The displacing and displaced fluids are considered to be incompressible and immiscible. In addition, we ignore the effects of capillarity and gravity in our simulations. We assume the displacement is isothermal and no source or sink exists in the domain. Therefore, the governing equations for flow are described by the conservation of mass and Darcy's law as

$$\varphi \frac{\partial S_m}{\partial t} + \nabla . \underline{u}_m = 0 \tag{1}$$

$$\underline{u}_m = -\frac{K k_{rm}}{\mu_m} \nabla p \tag{2}$$

where φ is porosity, K is absolute permeability, p is pressure, t is time, S_m, $\underline{u}_m$, k_{rm}, and μ_m are saturation, Darcy velocity, relative permeability and viscosity of phase m. The saturation of the phases are constrained by

$$\sum_m S_m = 1 \tag{3}$$

By some algebraic manipulation and combining Equations (1), (2), and (3), the governing equations are converted to

$$\varphi \frac{\partial S_m}{\partial t} - \nabla . \left[\frac{K k_{rm}}{\mu_m} \nabla p \right] = 0 \tag{4}$$

$$\nabla.\left[\sum_m \left(\frac{Kk_{rm}}{\mu_m}\nabla p\right)\right] = 0 \tag{5}$$

Equation (4) and (5) are known as the saturation and pressure equations, respectively.

CVFE Method

We apply a control volume finite element (CVFE) approach in conjunction with an implicit pressure explicit saturation (IMPES) method to discretize the pressure and saturation equations in space and time. In the CVFE approach, the pressure and saturation are represented using finite element and control volume basis functions, respectively,

$$p = \sum_j \hat{p}_j N_a \tag{6}$$

$$S = \sum_j \hat{S}_j M_b \tag{7}$$

where N_a is first order finite element basis function, M_b is control volume basis function that is equal to unity over the control volume constructed around node *j* (Figure 1) and is equal to zero everywhere else. The $\hat{p}_j$ and $\hat{S}_j$ are the nodal values for pressure and saturation, respectively.

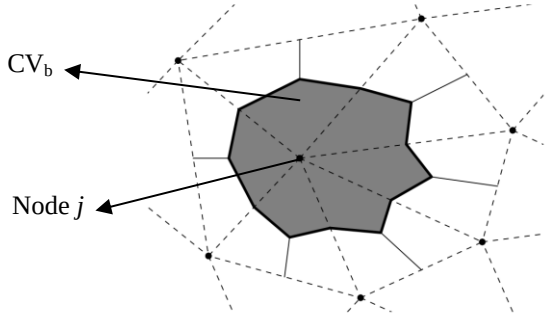

Figure 1. The control volume (CV_b) constructed around node *j* is shown in gray. Dotted lines show the elements boundaries.

To generate a linear system for pressure, a Petrov-Galerkin weighted residual method is used. Equation (5) is multiplied by a control volume based weight function and is integrated over the computational domain,

$$\int_\Omega M_b \nabla \cdot \left(\sum \left(\frac{Kk_{rm}^n}{\mu_m} \nabla p^{n+1} \right) \right) dV = 0 \tag{8}$$

where superscripts *n* and *n+1* denote the current time and the next time step, respectively. Note that due to the use IMPES time discretization, the relative permeability is calculated based on saturation at time step *n*.

M_b is a control volume wise function that is equal to unity only over control volume *b*, therefore,

$$\int_{\Gamma_{CV_b}} \underline{n} \cdot \left(\sum_m \left(\frac{Kk_{rm}^n}{\mu_m} \nabla p^{n+1} \right) \right) d\Gamma = 0 \tag{9}$$

where all terms are calculated at the control volume surfaces. For calculation of face values of relative permeability, an upwind scheme is applied. Substituting for pressure from Equation (6), a linear set of equation is formed that is solved using a GMRES method (Saad and Schultz, 1986).

To update saturation, Equation (4) is used and by applying standard node centered control volume weighting and basis functions we obtain

$$\int_{\Omega_{CV_b}} \frac{\phi S_m^{n+1}}{\Delta t} dV = \int_{\Gamma_{CV_b}} \underline{n} \cdot \left(\frac{Kk_{rm}^n}{\mu_m} \nabla p^{n+1} \right) d\Gamma + \int_{\Omega_{CV_b}} \frac{\phi S_m^n}{\Delta t} dV \tag{10}$$

The saturation equation is solved explicitly following solving for pressure at each time. For more details regarding the applied numerical method, refer to Mostaghimi et al. (2014) and Jackson et al. (2015).

Dynamic Mesh Adaptivity

Numerical discretization produces numerical error in resolving the curvature of a smooth solution. As the curvature increases, a finer mesh is required to control the error. In this work, mesh optimization is initiated by estimating the L_2 norm of local interpolation error in saturation using the Hessian matrix. Galerkin projection is used to project the variables defined in the control volume space onto finite element space. Although there is no proof that the upper bound of the interpolation error is bounded using this approach, various practical applications suggest that this is the case, at least for the linear interpolation error The Hessian is calculated by iterative Galerkin projection of the linear interpolation as in Loseille and Alauzet (2011). and then a functional prescribing mesh quality is defined for a finite element partitioning of the domain such that

$$I = \sum_{i \in edges} (v_i^T M v_i - 1)^2 \tag{11}$$

where I is the functional, v_i is vector describing the edges connecting the vertices of the finite element mesh, and

$$M_{ij} = \big(det(H)\big)^{-\frac{1}{2\gamma+\delta}} \frac{|H_{ij}|}{\epsilon} \tag{12}$$

defines the matrix describing the interpolation error metric along each edge (Chen et al 1997). H is the Hessian matrix of the solution, ϵ is a normalizing factor, effectively specifying the desired tolerance in the chosen field, γ is the polynomial degree for the chosen norm that is specified to be 2, and δ is the dimension of the problem. The mesh adaptivity process is reduced to minimizing the functional, I, and thus to generating a mesh with a minimum (and thus approximately uniform) interpolation error estimate. Additional bounds are defined to control the size of the constructed new meshes at each time step including minimum and maximum edge length. These constraints contribute in generating a unified metric field specifying the preferred anisotropic mesh resolution. Based on the target metric, the local structure mesh is modified iteratively in the areas where the current resolution of mesh has a higher interpolation error than what is desired. This results in refinement and coarsening of the mesh until the required length scales are obtained or no further improvement is possible. The mesh adaptivity modifies the existing mesh in each time step through topological operations including:

1. Refinement via splitting existing elements and adding additional degrees of freedom along an existing edge and regenerating the existing elements that share it.
2. Coarsening by edge collapse, removing an existing degree of freedom by collapsing an existing edge to zero length and thus replacing two vertices by a single one lying at the edge midpoint.
3. Face-edge and edge-face swaps, reordering the connectivity of existing groups of elements to improve the mesh shape, as measured by the functional.
4. Node movement, repositioning a vertex within the convex hull spanned by the elements that share it.

Following construction of the new mesh satisfying the specified constraints, variables are transferred from the previous mesh structure to the new one. This is realized by applying a conservative Galerkin projection-interpolation technique (Farrell, 2011). The relative permeability functions are recalculated based on the local recalculated saturation similar to that of commercial simulator with fixed grids.

Further discussions relating to the significance of dynamic mesh adaptivity in improving the numerical dispersion error for prediction of saturation can be found in Pain et al. (2001) and Mostaghimi et al. (2015).

Numerical Simulations

We simulated incompressible, immiscible, two-phase displacements in a two dimensional, horizontal, rectilinear porous medium. The medium has dimensions of 100×100 m^2 and the rock and fluid properties are taken from Jauré et al. (2014), which in turn were based on the experiments reported by Riaz et al. (2007). The model reservoir was assumed to be homogeneous with uniform porosity and permeability of 20.5% and 377 *mD*, respectively. The relative permeabilities in all the models were calculated as a quadratic function of saturation, giving a shock front mobility ratio of 100 for the oil and water viscosities used (Table 1). Water, as the displacing fluid, was injected with a constant velocity of 10^{-6} m/s along the left hand side while a constant pressure boundary condition was applied on the outlet, i.e. the right hand side boundary. These were modeled using horizontal injection and production wells located along the left and right hand sides of the reservoir. The wells were perforated in all grid blocks along the boundary. No-flow boundaries were imposed on the remaining sides. We assumed Newtonian flow behaviour. The rock and fluid properties used in all simulations are summarized in Table 1. Gravity and capillary pressure were ignored.

Table 1. Rock and fluid properties

Porosity (%)	20.5
Permeability (mD)	377
Water viscosity (Pa S)	0.001
Oil viscosity (Pa S)	0.1
Water relative permeability	$k_{rw}=S_w^2$
Oil relative permeability	$k_{ro}=(1-S_w)^2$

We compared the results from our CVFE simulations, both with and without mesh adaptivity, with results obtained from the black oil commercial simulator Eclipse 100 (Schlumberger, 2013). Eclipse uses a finite volume discretization and a fixed mesh. An IMPES solution was used in both models.

The range of meshes, resolutions and simulators employed are summarized in Tables 2 and 3. We first investigated the impact of mesh resolution and orientation on the fingering patterns predicted by Eclipse. Meshes 1 and 2 were uniform with 100×100 and 1000×1000 cells, respectively. To study the effects of non-uniform gridding on the fingering pattern two extra models were generated. In these two models (Meshes 3 and 4), the medium was divided into two equal regions (left and right). The left region was connected to the injection well and the right region was in contact with the production well. In Mesh 3, the left region was uniformly discretized with a grid block size of 1×1 m^2 while the right region consisted of finer grid blocks of 0.1×0.1 m^2. In Mesh 4, we used a higher resolution grid (0.1×0.1 m^2 grid blocks) for the left region while the right region consisted of a lower resolution grid (1×1 m^2 grid blocks). In all these models the grid was orientated parallel to the main direction of flow.

To investigate the importance of mesh orientation on viscous fingering, we also used a diagonal mesh arrangement. This was Mesh 5. To build Mesh 5 in the commercial simulator, we created a uniformly meshed Cartesian grid formed of 1415×1415 grid blocks. Each grid block was 0.1×0.1 m^2. The central region of the grid (Figure 2), with dimensions 100×100 m^2, was given a porosity of 20.5% and a permeability of 377 *mD* and the rest of the grid blocks were set to be inactive. The injection and production wells were located on the two opposite sides of the selected region as shown in Figure 2.

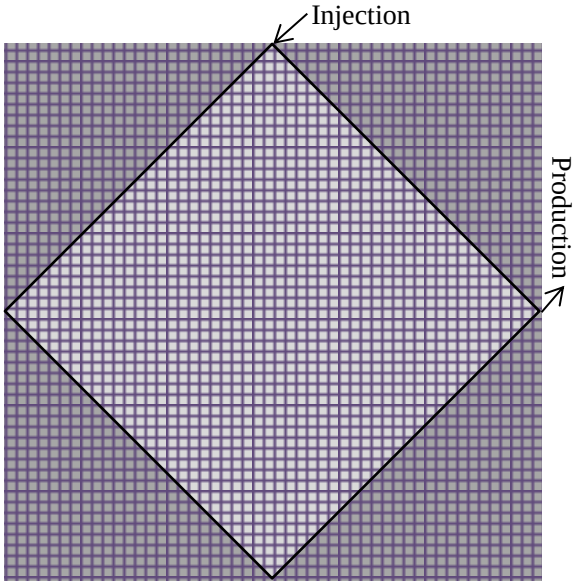

Figure 2. Wells arrangement for constructing Mesh 5 with diagonal mesh. The dark gray sections represent the inactive regions of the porous medium that do not contribute to the displacement.

We compared the results of simulations from Meshes 1 to 5 with those obtained from our CVFE simulator using both static and dynamic meshes. Meshes 6 and 7 used static structured and unstructured triangular meshes, respectively and were designed to investigate the possible effect of mesh orientation when using the CVFE discretization. Figure 3 shows a schematic of the meshes created for all these cases. Mesh 8 used a dynamic, adaptive anisotropic mesh after the displacing fluid had passed through 20% of the medium. Before this, it used a fixed mesh with each cell having a characteristic length of 0.1 *m* to allow fingers to begin to form and grow. The minimum and maximum edge length are specified as 0.1*m* and 50*m*, respectively. The minimum length is chosen such that the highest resolution of mesh created during mesh adaptation is consistent with other models (Meshes 2, 6 and 7) and the maximum edge length is chosen to be half the domain size. The mesh adaptation occurs after each time step. Metric advection is also applied to predict the future density of mesh and to enable the method to capture the propagation of instabilities in the saturation front.

For both sets of simulations, using the commercial simulator and the CVFE method, a fixed time step of 1800 seconds was used. All simulations were performed on a PC with a 3.2 GHz CPU with no parallel processing.

The viscous fingers were triggered using a random initial water saturation in the first row of grid blocks adjacent to the injection well. This had a variance of 10% and a wavelength of 1 *m* .

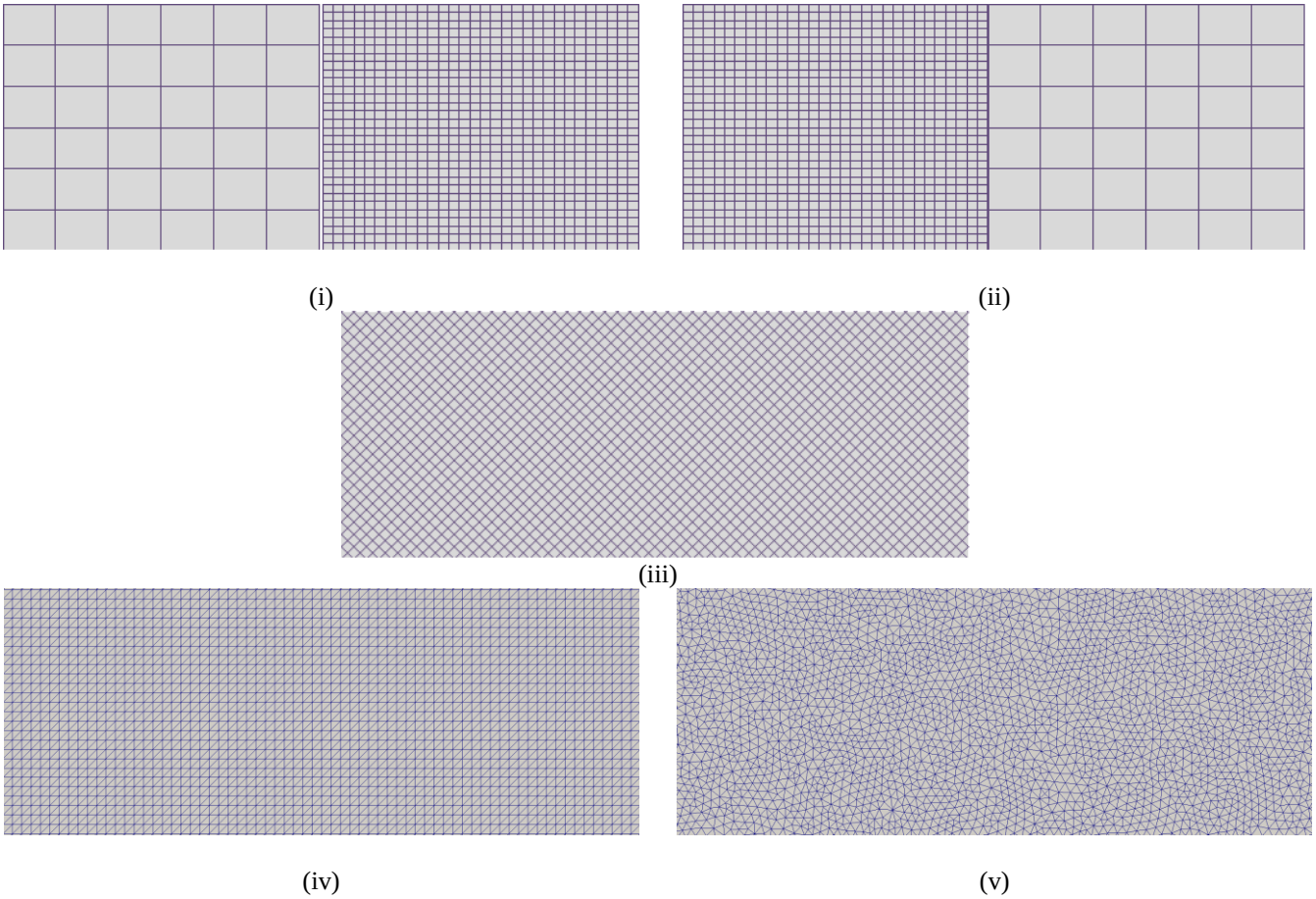

Figure 3. A schematic of the non-uniform parallel Cartesian meshes used for Meshes 3 and 4 (i, ii), diagonal mesh used for Mesh 5 (iii), structured (iv) and unstructured (v) triangular elements used for Meshes 6 and 7, respectively.

Results

Stable Displacement

The CVFE model was first validated by comparing its predictions using both a fixed two dimensional mesh and a dynamic adaptive two dimensional mesh with the Buckley-Leverett solution (Buckley and Leverett, 1941) for a simulation in which fingers were not triggered. The simulations were also performed using the commercial simulator. The fluid and rock properties are as shown in Table 1. Figure 4 shows the saturation profiles along the horizontal line at y=50 m and at 0.08 PVI. The analytical solution is also displayed.

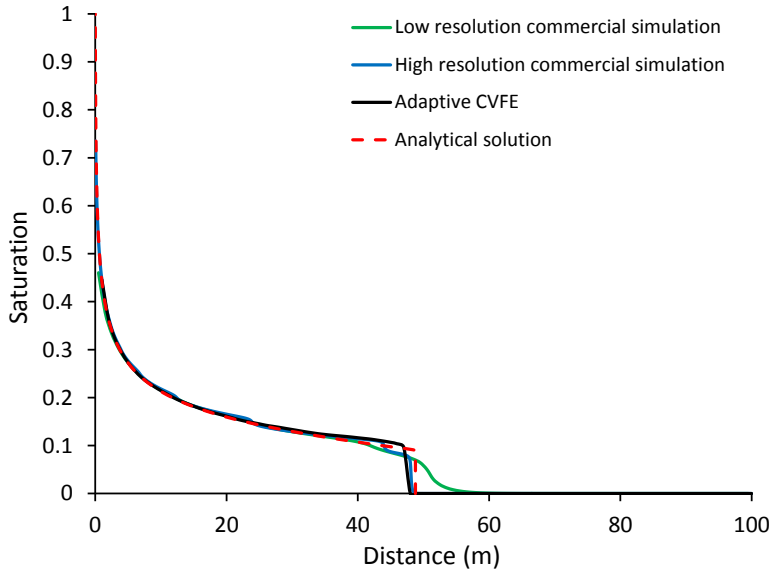

Figure 4. Comparison of numerical simulation results with the Buckley-Leverett analytical solution for 1D flow without fingering, showing saturation profiles from the low and high resolution commercial simulations and adaptive CVFE simulation. The analytical solution is shown with a dashed line. The high and low resolution finite volume meshes had 1,000 and 100 grid blocks in the main direction of flow, respectively. The adaptive CVFE mesh had 1330 elements.

The accuracy of any simulator obviously depends on the mesh resolution. The saturation profile obtained from the coarser grid commercial simulation suffers from a significant numerical dispersion error and does not capture a sharp saturation profile. The results obtained from adaptive CVFE simulation are very similar to results from the higher resolution commercial simulation. The high resolution commercial model had 1,000×1,000 grid blocks whilst the adaptive model had only 1330 elements.

In the adaptive mesh simulation, a high resolution mesh was formed in the vicinity of the displacement front, with the aim of minimizing numerical diffusion error. Figure 5 (i) shows the saturation distribution for the Buckley-Leverett validation shown in Figure 4, whilst Figure 5 (ii) shows the mesh used to create the distribution in Figure 5 (i). The CPU time for the low resolution and high resolution commercial simulations was 23 and 9983 seconds, respectively. The adaptive mesh required only 234 seconds, which is much lower than that required by the high resolution model whilst offering similar accuracy. Mostaghimi et al. (2015) has provided further more test cases for validation of the developed CVFE method and Mostaghimi et al. (2014) demonstrated that the static mesh CVFE discretization has a linear order of convergence.

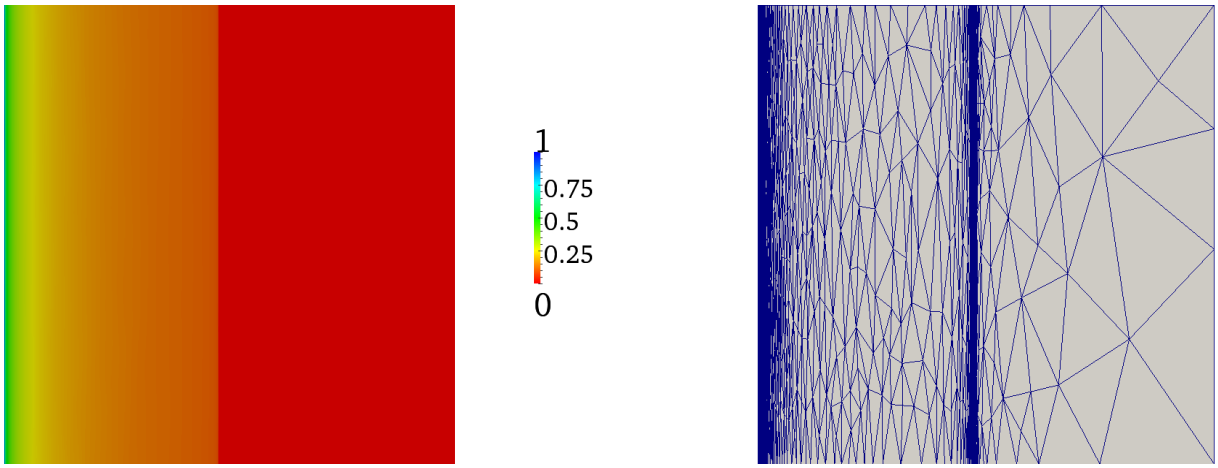

(i) (ii)

Figure 5. (i) Saturation distribution in the adaptive CVFE simulation of Buckley-Leverett displacement shown in Figure 4. (ii) The mesh generated at this instant in simulation time .

Unstable Displacement

Next, we used the initial disturbance discussed in the previous section to trigger fingers and compared the solutions of adaptive mesh simulation with those obtained using the commercial simulator for several different grid resolutions and types of meshes. The same disturbance was used in all cases. Figure 6 compares the fingering patterns seen in the different meshes at early time (0.03 PVI).

Figures 6 (i) to (v) show results from the commercial simulator whilst Figures 6 (vi) and (viii) show those from the CVFE simulator. The effect of mesh resolution can clearly be seen in Figures 6 (i) and 6 (ii). The higher the mesh resolution, the greater the number of fingers. This is in agreement with the growth rate analysis described by a number of authors including Christie (1989) for miscible viscous fingering and Chikhliwala et al. (1988). In the absence of transverse diffusion (miscible viscous fingering) or transverse capillary pressure, the growth rate of viscous fingers increases with their wavenumber. In the finite volume simulations of immiscible displacement studied here, it appears that the maximum wavenumber (minimum wavelength) simulated corresponds approximately to the number of grid blocks perpendicular to flow when the grid is orientated parallel to flow e.g. in Mesh 1, the number of fingers is approximately 50 while for Mesh 2 we observe hundreds of fingers. In contrast, in previous studies of miscible viscous fingering the minimum width of each finger in the absence of transverse diffusion is several grid blocks. The number of fingers seen in Meshes 1 and 3 at early time is also very similar in number suggesting that mesh resolution ahead of the saturation front does not influence the fingering pattern. The same observation is true for Meshes 2 and 4 where the low resolution of mesh in Mesh 4 in front of the saturation front has negligible impact on the fingering pattern.

The effect of grid orientation on the fingering pattern can be seen by comparing Figures 6 (i) (when the grid is parallel to flow) and Figure 6 (v) (when the grid is diagonal to the principal flow direction). It can be seen that the fingers are thicker and fewer in number when the grid is diagonal to the principal flow direction. This is because the diagonal grid introduces a

transverse numerical diffusion that results in a maximum growth rate for a particular wavenumber of fingering (Yortsos and Huang, 1986). It should be remembered that Meshes 2 and 5 have similar mesh resolution and the only reason for different saturation distribution is the different grid orientation and hence different numerical diffusion. Figures 6 (vi) and 6 (vii) show the saturation distributions using the CVFE simulator. The fingering patterns in these simulations are very similar for different mesh orientations with similar resolution. This suggests that the CVFE does not suffer from such a large grid orientation error as the finite volume schemes but conversely this does cause a higher transverse numerical diffusion. Figure 6 (viii) shows a result using mesh adaptivity that is in excellent agreement with the static meshes but requires much fewer elements.

Figure 7 shows the evolution of fingers at a later time (0.13 PVI). In the uniform Cartesian grid Meshes 1 and 2, some of the numerical fingers merge, however, they are still numerous and their width is of the order of a grid block. In Mesh 3, as the mesh resolution is finer in the right hand region of the model, tip splitting occurs triggered by finer grid and the lack of transverse numerical or physical diffusion. Fingers that were captured by a single grid block at the early time of simulation, now occupies 10 grid blocks. Due to the high mobility of the displacing fluid and the increased resolution, finer fingers can be resolved and their growth rate is higher than the longer wavelength fingers.. In contrast, for Mesh 4, the mesh resolution decreases in the right hand region. Therefore, the numerical fingers merge and the number of formed fingers is similar to those in Mesh 1. As noted above, in all Meshes 1-4, the number of fingers is directly related to the mesh resolution in the region they grow. The width of fingers in these models is at the scale of the grid block size in the right hand region. Figure 7 (v) shows the evolution of fingers on the diagonal grid, as simulated by the finite volume method. In this model, the width of each finger is approximately 50 grid blocks, which is significantly higher than in the parallel grid models.

Figures 7 (vi) and (vii) show the CVFE results for the fingering pattern in the static structured and unstructured triangular meshes, respectively. These two patterns of fingers are very similar while their mesh formats are different. They are also similar to those seen using Mesh 5 in the finite volume simulator. Figure 7 (viii) shows the saturation distribution and fingering pattern obtained when using dynamic mesh adaptivity. Qualitatively, the fingering pattern and size are similar to Meshes 5-7. However, the number of fingers in the adaptive mesh is slightly less than Meshes 6 and 7. This is probably due to the interpolation error occurring during mesh adaptation.

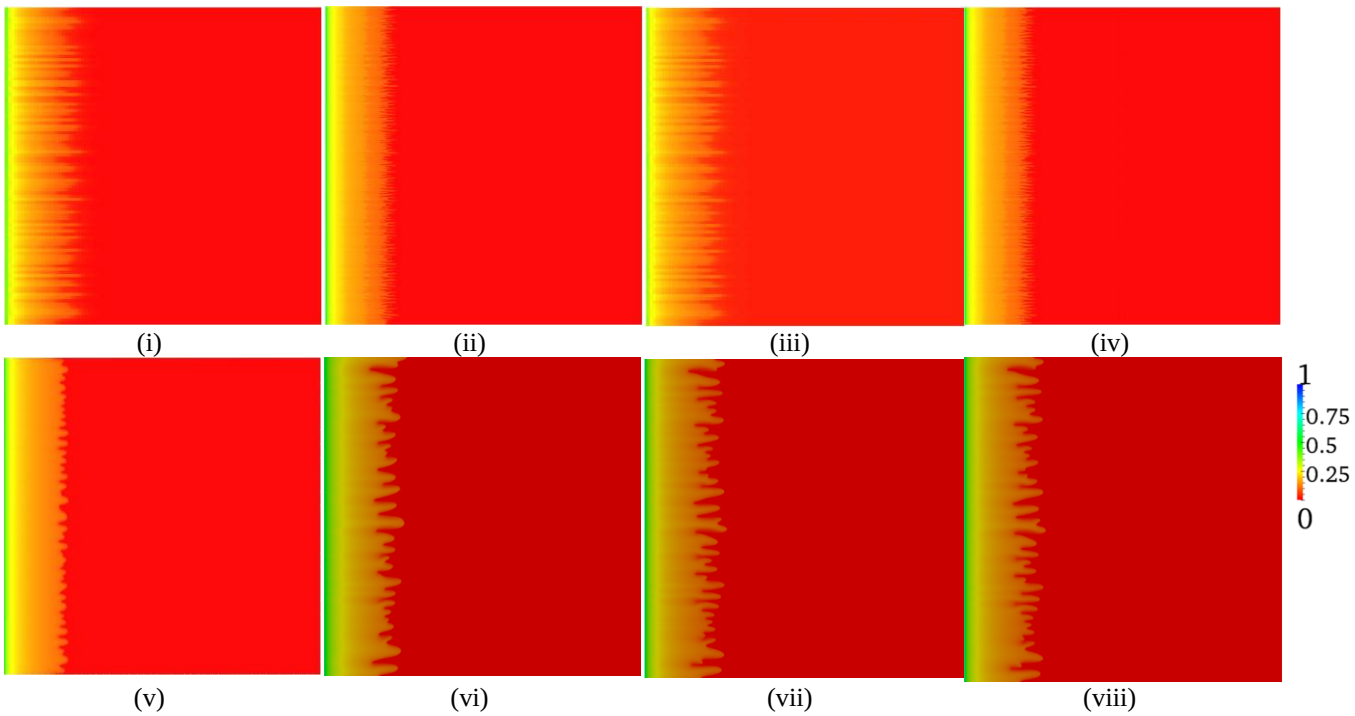

Figure 6. Fingering patterns at 0.03 PVI for Mesh 1 with uniform parallel low resolution mesh (i), Mesh 2 with uniform parallel high resolution mesh (ii), Mesh 3 with non-uniform parallel mesh consisting of low resolution mesh in the left region and high resolution mesh in the right region (iii), Mesh 4 with non-uniform parallel mesh consisting of high resolution mesh in the left region and low resolution mesh in the right region (iv), Mesh 5 with diagonal uniform mesh (v), Mesh 6 with structured triangular mesh (vi), Mesh 7 with unstructured triangular mesh (vii), and Mesh 8 with anistropic adaptive mesh (viii).

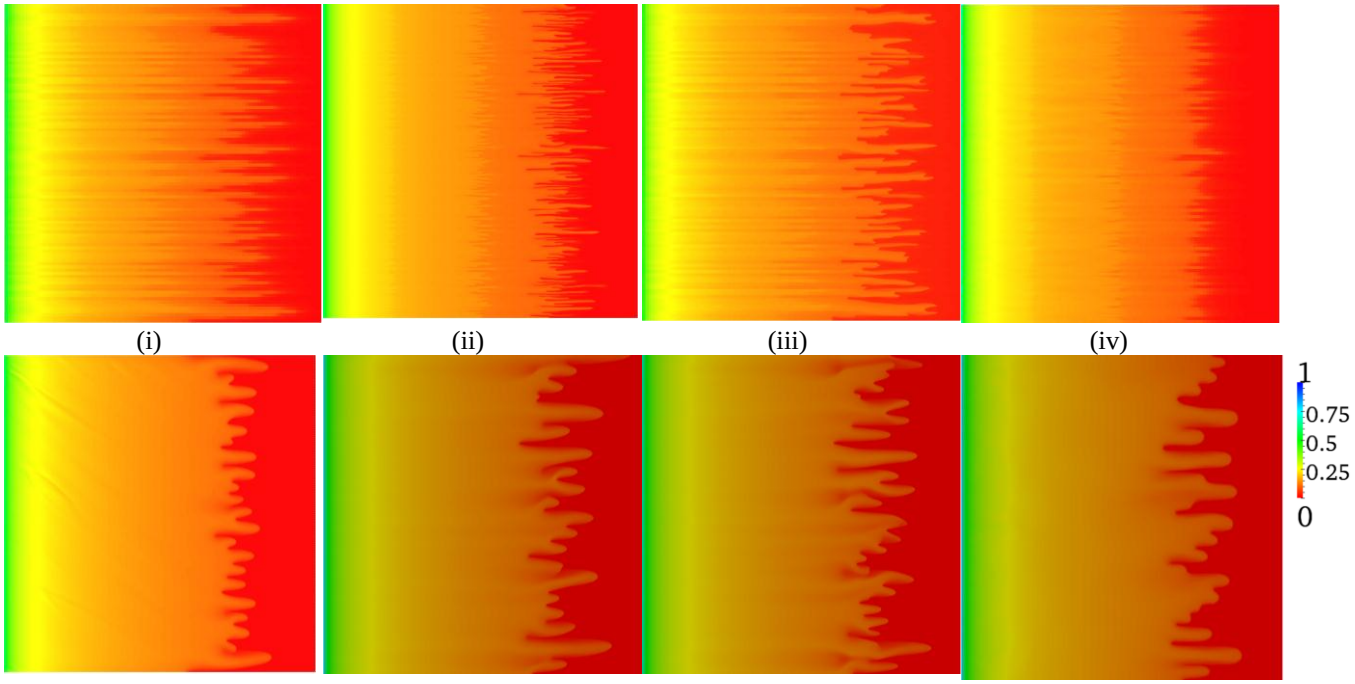

Figure 7. Fingering patterns at 0.13 PVI for Mesh 1 with uniform parallel low resolution mesh (i), Mesh 2 with uniform parallel high resolution mesh (ii), Mesh 3 with non-uniform parallel mesh consisting of low resolution mesh in the left region and high resolution mesh in the right region (iii), Mesh 4 with non-uniform parallel mesh consisiting of high resolution mesh in the left region and low resolution mesh in the right region (iv), Mesh 5 with diagonal uniform mesh (v), Mesh 6 with structured triangular mesh (vi), Mesh 7 with unstructured triangular mesh (vii), and Mesh 8 with anistropic adaptive mesh (viii).

Figures 8 (i) and (ii) show the meshes generated for Mesh 8 after 0.03 and 0.13 PVI, respectively. The minimum edge length of elements is 0.1 *m* (similar to the grid block size in the high resolution grid in Meshes 2 and 5). On the other hand, the maximum allowed number of elements is 10,000, which is similar to the lower resolution mesh in Mesh 1. The dynamic mesh adaptivity generates a higher resolution mesh in the areas where fingers are growing and coarsens mesh in other regions. As can be seen in Figure 8 (i), the edge length of elements ahead of the saturation front increases up to 50 *m* while the refined mesh close to fingers have an edge length of 0.1 *m*.

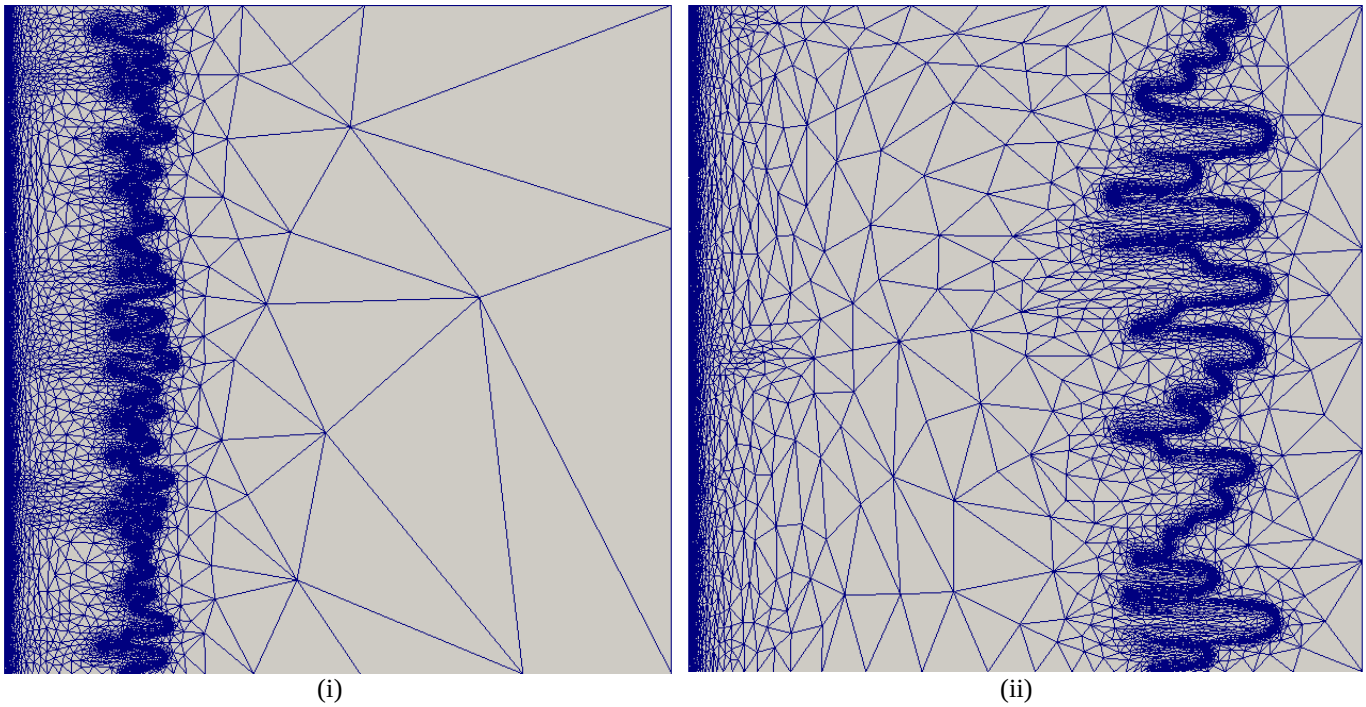

Figure 8. Anisotropic meshes generated for Mesh 8 at 0.03 (i) and 0.13 (ii) PVI.

Table 2. Mesh properties of Models 1-7, computational time, and breakthrough time						
	Mesh format	$n_x \times n_y$	dx×dy (m)	n_{total}	CPU time (hours)	Breakthrough time (PVI)
Mesh 1	Uniform parallel Cartesian	100×100	1×1	10,000	0.12	0.135
Mesh 2	Uniform parallel Cartesian	1000×1000	0.1×0.1	1,000,000	25.8	0.145
Mesh 3	Non-uniform parallel Cartesian	50×100+500×1000	1×1/0.1×0.1	505,000	7.7	0.135
Mesh 4	Non-uniform parallel Cartesian	500×1000+50×100	0.1×0.1/1×1	505,000	40.6	0.147
Mesh 5	Uniform diagonal	1000×1000	0.1×0.1	1,000,000	174.9	0.158
Mesh 6	Structured triangular	1000×1000	0.1*	2,000,000	509.2	0.148
Mesh 7	Unstructured triangular	1000×1000	0.1*	2,000,000	523.4	0.148

*denotes the characteristic length of elements

	Table 3: Mesh properties for Mesh 8, computational time, and breakthrough time				
Mesh format	Minimum value for length of elements (m)	Maximum value for length of elements (m)	Maximum number of elements	CPU time (hours)	Breakthrough time (PVI)
Adaptive	0.1	50	10,000	22.4	0.152

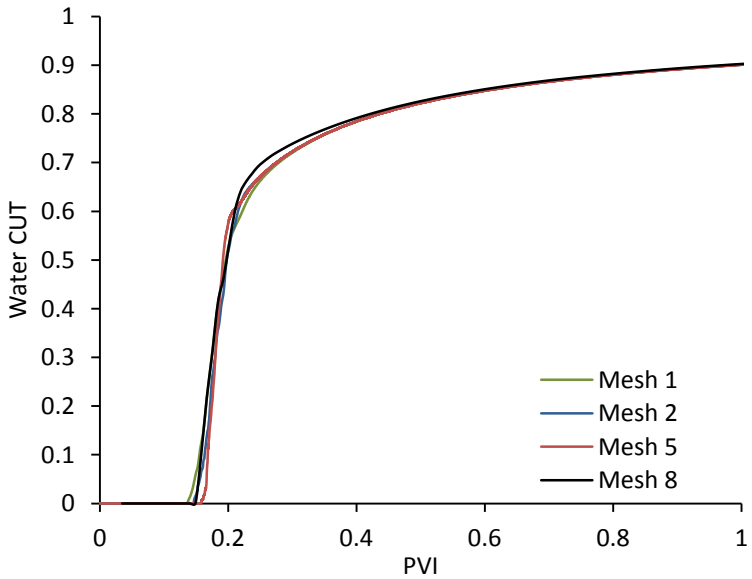

Figure 9. Watercut as function of PVI for Meshes 1, 2, 5, and 8.

The breakthrough times (calculated when the watercut exceeds 10^{-4}) obtained using the different meshes and simulation models are reported in Table 2 and Figure 9 shows the watercut as a function of time when using Meshes 1, 2, 5 and 8. The results for Meshes 6 and 7 are very similar to those obtained using Mesh 8 and are not shown on Figure 9. They are all very similar. The finite volume simulations using Meshes 1 and 3 predict the earliest breakthrough whilst that using mesh 5 predicts the latest breakthrough time. The breakthrough times predicted by the three CVFE simulations (Meshes 6, 7 and 8) are very similar to those predicted by the finite volume simulation using Meshes 2 and 4. The fingering pattern in terms of wavelength is very similar in all the CVFE simulations so we expect a similar growth rate for the fingers and thus a similar breakthrough time. On the basis of the growth rate analysis of Chikhliwala et al. (1988), we would have expected Mesh 2 (which has the highest wavenumber fingers and the lowest level of numerical diffusion) to break through earlier than the Mesh 1 simulations as these should have the highest growth rate. This is not the case. Instead it seems that the increased

levels of longitudinal numerical diffusion in the Mesh 1 (coarse) simulations outweigh the difference in growth rate causing the Mesh 1 simulations to breakthrough earlier.

The computational time after 2 PVI for all simulations is also given in Table 2. As expected, the computational time increases as the mesh becomes finer. The computational time for Mesh 2 is approximately 208 times higher than Mesh 1. Mesh 5 requires more iterations to converge and requires a longer computational time in comparison with Mesh 2. For Meshes 3 and 4, the computational time is between Meshes 1 and 5. The computational time for Mesh 8 is lower than Model 2 and 5 while its accuracy is similar. The CPU time for Meshes 6 and 7 is approximately 20 times higher than for Mesh 2 showing the additional computational effort needed to solve a CVFE model (although it should be noted all these simulations were run on a single processor and CVFE methods lend themselves to more efficient parallelization than finite volume techniques). Mesh 8 runs 24 times more quickly than Meshes 6 and 7, highlighting the efficiency of mesh adaptivity. In future work, more efforts will be made to optimize the computational time for both the CVFE code and the mesh adaptivity to make it significantly faster than the commercial simulator while not losing accuracy.

Conclusions

Recent investments in waterflooding of heavy oil reservoirs have renewed interest in the simulation of viscous fingering in immiscible displacements. One of the main factors affecting accurate simulation of fingering is the choice of mesh size and orientation in order to ensure that the simulations are dominated by physical rather than numerical diffusion and grid to minimise grid orientation effects. Typically this means a very fine grid is needed, especially for field scale simulations where levels of physical diffusion are very low but this can result in very long simulation times.

We propose using an adaptive mesh, control volume, finite element (CVFE) method to resolve this phenomenon accurately and efficiently. Dynamic mesh adaptivity optimizes the mesh resolution based on fingering structures whilst the use of a CVFE approach reduces the grid orientation error seen in finite volume simulations. We have compared the size and pattern of fingering obtained by this method with results of a commercial reservoir simulator based on finite volume methods using models with parallel, diagonal and non-uniform gridding. Our results indicate that there was a significant grid orientation error associated with the finite volume approach. A very different fingering pattern was seen depending upon whether a parallel and diagonal grid was used. The diagonal grid resulted in fewer fingers, probably because of higher levels of numerical diffusion, although predicted watercut versus time was similar in both cases.

The water cut profile obtained from the adaptive CVFE approach agreed well with the results from the conventional commercial simulator . The fingering pattern obtained from the CVFE approach agreed best with that seen when using a diagonal grid in the finite volume simulations on a fixed grid for both static and adaptive meshes, suggesting that the level of transverse numerical diffusion was similar in both cases. The simulation time obtained when using a dynamic and adaptive mesh was significantly faster than that needed for the fine, fixed mesh, CVFE simulations and comparable to that needed for the fine grid runs using the commercial simulator. This was despite the fact that this code has not yet been optimized. We expect the CPU time for this approach to reduce once this has been done. Further work is also needed to validate the models against experiments and analytical results when there is capillary pressure present.

Acknowledgements

TOTAL is thanked for initiating this research and for partial financial support of Jackson and Muggeridge under the TOTAL Chairs program at Imperial College London. Pain acknowledges support from EPSRC funds ‘Multi-Scale Exploration of Multiphase Physics in Flows – MEMPHIS’ and ‘Computational Modelling for Advanced Nuclear Power Plants’.

References

Araktingi, U. G., and Orr Jr, F. M. 1993.Viscous fingering in heterogeneous porous media. *SPE Advanced Technology Series*, 1(01), 71-80.

Berg, S., and Ott, H. 2012. Stability of CO2–brine immiscible displacement. *International Journal of Greenhouse Gas Control*, 11, 188-203.

Blackwell, R. J., Rayne, J.R. and Terry W.M. 1959. Factors influencing the efficiency of miscible displacement. *AIME*, 217, 1-8.

Buckley, S. E., and Leverett, M. C. 1941. Mechanism of fluid displacement in sands. *Trans AIME* 146(1337):107–116.

Chen, L., Sun, P., Xu, J. 2007. Optimal anisotropic meshes for minimizing interpolation errors in *Lp*-norm. *Mathematics of Computation*, 76(257), 179-204.

Christie, M. A., and Bond. D.J. 1987. Detailed simulation of unstable processes in miscible flooding. *SPE Reservoir Engineering*. 2 (04), 514-522.

Christie, M. A., and Jones. A.D.W.1987. Comparison between laboratory experiments and detailed simulation of miscible viscous fingering. 4th European Symposium on Enhanced Oil Recovery.

Christie, M. A. 1989. High-resolution simulation of unstable flows in porous media. *SPE Reservoir Engineering*, 4(03), 297-303.

Chikhliwala, E.D., Huang, A.B., Yortsos, Y C. 1988. Numerical study of the linear stability of immiscible displacement in porous media. *Transport in Porous Media*, 3(3), 257-276.

Christie, M. A., Muggeridge, A. H., and Barley, J. J. 1993. 3D simulation of viscous fingering and WAG schemes. *SPE Reservoir Engineering*, 8(01), 19-26.

Chuoke, R.L., Van Meurs, P., van der Poel, C. 1959. The instability of slow, immiscible, viscous liquid-liquid displacements in permeable media. In SPE Annual Fall Meeting. Society of Petroleum Engineers, SPE paper 1141.

Daripa, P., and Paşa, G. 2008. On capillary slowdown of viscous fingering in immiscible displacement in porous media. *Transport in Porous Media*, 75(1), 1-16.

Davies, G. W., Muggeridge, A. H. and Jones. A.D.W. 1991.Miscible displacements in a heterogeneous rock: detailed measurements and accurate predictive simulation. SPE Annual Technical Conference and Exhibition. Society of Petroleum Engineers, SPE Paper 22615.

De Wit, A., and Homsy, G.M. 1997. Viscous fingering in periodically heterogeneous porous media. II. Numerical simulations. *The Journal of Chemical Physics*, 107(22), 9619-9628.

Djjabarov, S., Jones, A.D.W., Krevor, S. and Muggeridge, A.H. 2016. Experimental and numerical Studies of first contact miscible injection in a quarter five spot pattern". To be presented at SPE Europec, Paper SPE180125.

Edwards, M, and Chrisitie, M. A. 1993. Dynamically adaptive godunov schemes with renormalization in reservoir simulation. In SPE Symposium on Reservoir Simulation. Society of Petroleum Engineers, SPE paper 25268.

Farrell, P. E. 2011. The addition of fields on different meshes. *Journal of Computational Physics*, 230(9), 3265-3269.

Jaure, S., Moncorge, A., de Loubens, R. 2014. Reservoir Simulation Prototyping Platform for High Performance Computing. In SPE Large Scale Computing and Big Data Challenges in Reservoir Simulation Conference and Exhibition. Society of Petroleum Engineers, SPE paper 172989.

Jackson, M.D., Percival, J., Mostaghimi, P., Tollit, B., Pavlidis, D., Pain, C., Gomes, J., Elsheikh, A.H., Salinas, P., Muggeridge, A. and Blunt, M., 2015. Reservoir modeling for flow simulation by use of surfaces, adaptive unstructured meshes, and an overlapping-control-volume finite-element method. *SPE Reservoir Evaluation & Engineering*, 18(2), 115-132.

Kelkar, M., and Gupta, S. P. 1991. A numerical study of viscous instabilities: Effect of controlling parameters and scaling considerations. *SPE Reservoir Engineering*, 6(01), 121-128.

Lake, L. W. 1989. *Enhanced oil recovery*. Prentice Hall, New Jersey.

Loseille, A., Alauzet, F. 2011. Continuous mesh framework part I: well-posed continuous interpolation error. *SIAM Journal on Numerical Analysis*, 49(1), 38-60.

Mostaghimi, P., and Mahani, H. 2010. A quantitative and qualitative comparison of coarse-grid-generation techniques for modeling fluid displacement in heterogeneous porous media. *SPE Reservoir Evaluation & Engineering*, 13(01), 24-36.

Mostaghimi, P., Percival, J.R., Pavlidis, D., Ferrier, R.J., Gomes, J.L., Gorman, G.J., Jackson, M.D., Neethling, S.J., and Pain, C.C. 2015. Anisotropic mesh adaptivity and control volume finite element methods for numerical simulation of multiphase flow in porous media. *Mathematical Geosciences*, 47(4), 417-440.

Mostaghimi, P., Tollit, B. S., Neethling, S. J., Gorman, G. J., and Pain, C. C. 2014. A control volume finite element method for adaptive mesh simulation of flow in heap leaching. *Journal of Engineering Mathematics*, 87, 111-121.

Mudler, W. A., and Gmeling Meyling, R. H. 1993. Numerical Simulation of two-phase flow using locally refined grids in three space dimensions, *SPE Advanced Technology Series*, 1(01), 36-41.

Muggeridge, A. H., Jackson, M. D., Al-Mahrooqi, S., Al-Marjabi, M., & Grattoni, C. A. 2002. Quantifying Bypassed Oil in the Vicinity of Discontinuous Shales. SPE Annual Technical Conference and Exhibition. SPE paper 77487

Pain, C. C., Umpleby, A. P., De Oliveira, C. R. E., and Goddard, A. J. H. 2001. Tetrahedral mesh optimisation and adaptivity for steady-state and transient finite element calculations. *Computer Methods in Applied Mechanics and Engineering*, 190(29), 3771-3796.

Piggott, M. D., Farrell, P. E., Wilson, C. R., Gorman, G. J., and Pain, C. C. 2009. Anisotropic mesh adaptivity for multi-scale ocean modelling. *Philosophical Transactions of the Royal Society A: Mathematical, Physical and Engineering Sciences*, 367(1907), 4591-4611.

Riaz, A., Tang, G.Q., Tchelepi, H.A., Kovscek, A. R. 2007. Forced imbibition in natural porous media: Comparison between experiments and continuum models. *Physical Review E*, 75(3), 036305.

Riaz, A., and Tchelepi, H.A. 2006. Influence of relative permeability on the stability characteristics of immiscible flow in porous media. *Transport in porous media*, 64(3), 315-338.

Ruith, M., and Meiburg, E. 2000. Miscible rectilinear displacements with gravity override. Part 1. Homogeneous porous medium. *Journal of Fluid Mechanics*, 420, 225-257.

Saad, Y., and Schultz, M. H. 1986. GMRES: A generalized minimal residual algorithm for solving nonsymmetric linear systems. *SIAM Journal on scientific and statistical computing*, 7(3), 856-869.

Saffman, P.G., and Taylor, G. 1958. The penetration of a fluid into a porous medium or Hele-Shaw cell containing a more viscous liquid. *Proceedings of the Royal Society of London A: Mathematical, Physical and Engineering Sciences*, 245(1242), 312-329.

Schlumberger (2013) Eclipse 100 Reference Manual.

Tan, C. T., and Homsy, G.M.. 1988. Simulation of nonlinear viscous fingering in miscible displacement. *Physics of Fluids.* 31(6),1330-1338.

Tchelepi, H. A., and Orr Jr, F. M. 1994. Interaction of Viscous Fingering Permeability Heterogeneity and Gravity Segregation in Three Dimensions. *SPE Reservoir Engineering*, 9(04), 266-271.

Yortsos, Y.C., and Huang, A.B. 1986. Linear-Stability Analysis of Immiscible Displacement: Part 1-Simple Basic Flow Profiles, *SPE Reservoir Engineering*, 1(04), 378-390.